Accepted Manuscript

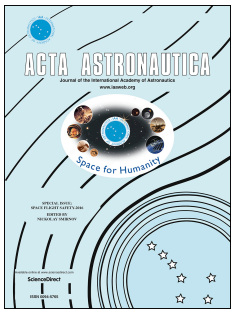

Ground-based experiment of capturing space debris based on artificial potential field

Zheng Huang, Yun Lu, Hao Wen, Dongping Jin

PII: S0094-5765(18)30619-2

DOI: 10.1016/j.actaastro.2018.08.017

Reference: AA 7053

To appear in: *Acta Astronautica*

Received Date: 29 March 2018

Revised Date: 8 July 2018

Accepted Date: 9 August 2018

Please cite this article as: Z. Huang, Y. Lu, H. Wen, D. Jin, Ground-based experiment of capturing space debris based on artificial potential field, *Acta Astronautica* (2018), doi: 10.1016/j.actaastro.2018.08.017.

This is a PDF file of an unedited manuscript that has been accepted for publication. As a service to our customers we are providing this early version of the manuscript. The manuscript will undergo copyediting, typesetting, and review of the resulting proof before it is published in its final form. Please note that during the production process errors may be discovered which could affect the content, and all legal disclaimers that apply to the journal pertain.

ACCEPTED MANUSCRIPT

Ground-Based Experiment of Capturing Space Debris Based on Artificial Potential Field

Zheng Huang, Yun Lu, Hao Wen[1], Dongping Jin

State Key Laboratory of Mechanics and Control of Mechanical Structures, Nanjing University of Aeronautics and Astronautics, Nanjing 210016, P.R. China

Abstract: An enabling debris capturing concept is experimentally demonstrated using an air-bearing testbed. To facilitate on-board implementation, the idea of artificial potential field is employed for the controller design of the debris capturing task. In particular, the artificial potential function is constructed such that all of its stable minima stratify the capturing condition, thereby avoiding the possibility of trapping into unwanted local minima. To experimentally simulate the mission of capturing space debris on ground, two air-bearing simulators are designed and developed, in which the first one is equipped with a single-degree-of-freedom robotic arm and the second one serves as a mock-up of the debris to be captured. The location and attitude of the simulators are measured by binocular cameras for control feedback. Experimental studies are performed to verify the results of the theoretic analysis.

Keywords: Space debris; Capture; Space robotic manipulator; Artificial potential field; Air-bearing testbed

[1]Corresponding author. Tel.:+86 025 84891672
E-mail address: wenhao@nuaa.edu.cn (Hao Wen)

1. Introduction

Since the first space exploration mission in 1957, space activities have created an orbital debris environment, especially in the geo-stationary orbit, which severely threatens the safety of orbiting satellites and sustainable space development [1-4]. Some space activities have significantly produced the enormous amounts of orbital space debris which may remain in orbit for many years and interfere with future space activities[5]. Because of the nearly geometric growth in the amount of the space debris, many investigators are of the opinion that the debris density at the Low Earth Orbit (LEO) has already reached a sufficiently high level to trigger a cascading event (Kessler Syndrome) [6].

As a result, space debris has been of deep concern to the entire international space community during recent decades. In contrast to on-orbit servicing missions, almost all space debris is characterized by non-cooperative and tumbling motion, with no reflectors, markers or radio beacons, which would help with determining the relative position and attitude [7]. Therefore, three of the most challenging tasks in active debris removal (ADR) are minimizing the impact influence, de-tumbling and attitude synchronization, all of which have been studied widely in recent years [8]. To alleviate this situation, many capturing methods have been proposed. These methods can be classified into two main categories: contact and contactless capturing methods. Contact capturing, the most commonly proposed method, includes tentacles-based capturing [9], robotic arm capturing [10] and net capturing [11], etc.

The robotic arm capturing method has attracted significant attention because of the advantages of stiff composite, higher Technology Readiness Level (TRL) technology and the capability of being easily tested on ground [8]. During the past decades, many kinds of the robotically capturing approaches have been proposed and investigated, however most of them mainly focus on theoretical and numerical studies [12]. Huang et al. established the impact dynamic model for target capturing and synthesized an adaptive control strategy to remove space debris by using a tethered space robot [13, 14]. Xu et al. proposed a method for autonomous rendezvous with a non-cooperative object in space, and developed a modeling and simulation system to verify the corresponding algorithms [15]. Lin et al. analyzed the polhode and tumbling frequency of the rotational space debris subjected to gravity-gradient torques and the orbit precession [16], which can be used to estimate the rotational state of the uniaxial space debris without any prior information except of the orbital parameters. Hu et al. proposed a trajectory planning algorithm capable of avoiding the configuration singularity of a space robot equipped with multiple manipulators [17].

Relatively less scholars have undertaken experimental research on this topic. For example, Dong and Zhu used a robotic arm installed on a fixed base to autonomously capture a mobile target with the help of visual servoing technique [18, 19], which required installing three non-collinear markers on the target at least. Moreover, many experimental studies using air-bearing spacecraft-simulator with robotic arm have also been reported. Toglia et al. demonstrated the control and sensing algorithms for assembly of spacecraft and space robots, based on the dual-arm two-link

spacecraft-simulator system floating on a testbed [20]. Boning et al. built multiple satellite-manipulator system mounted on air-bearing microgravity simulators, to verify the construction of a large space structure by two or more space robots [21]. Virgili-Llop et al. demonstrated an onboard implementable optimization-based guidance approach for the capture of tumbling objects by spacecraft equipped with a robotic manipulator on air-bearing testbed [22].

A typical mission for space debris capture may consist of rendezvous, measuring, capturing and de-tumbling phases. In light of the restrictions due to laboratory environment, this study primarily focuses on the capturing phase. To simulate the mission of capturing space debris on ground, two air-bearing simulators are designed and developed, in which the first one is equipped with a single-degree-of-freedom robotic arm and the second one serves as a mock-up of the debris to be captured. A potential-energy based controller is proposed to complete an autonomous capture of the target mock-up that floats on an air-bearing testbed. The artificial potential function of the controller is constructed such that all of its stable minima stratify the capturing condition, thereby avoiding the possibility of trapping into unwanted local minima. The proposed control scheme was validated experimentally through a successful capture of the mock-up of the debris.

The remainder of the paper is organized as follows. Section 2 describes the ADR problem of concern and the dynamic model of the ground-based experimental system. In Section 3, the design and stability analysis of the control law are presented. The experimental setup and results are given in Section 4. Finally, Section 5 draws the

conclusions of the paper.

2. Mission Concept and Dynamic Modeling

Figure 1 give a schematic description of the conceptual mission for debris capture, in which a specially designed robotic arm is installed on a platform and employed to capture a space debris. The bottom surface of the end effector of the robotic arm is covered with numerous tiny bristles, like gecko's foot, which could provide sufficient adhesion force for capturing debris. Previous studies showed that gecko foot hairs structure displayed excellent adhesion/release capacity even in the harsh space environment [23-25]. The bottom part (Disk A) of the end effector is connected via a revolute joint to the base part (Disk B) such that the relative rotation between the space debris and the end effector can be accommodated, where only single-axis rotation of space debris is considered for preliminary verification of conceptual feasibility.

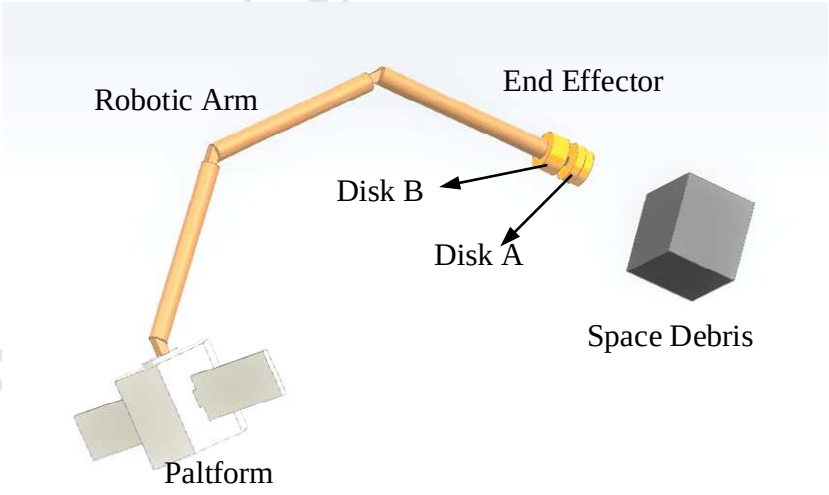

Fig. 1. Illustration of capturing active debris using a robotic arm

In this conceptual design, the space mission for active space debris capture includes the following four phases: the first step is the rendezvous phase in which the

spacecraft approaches from a relatively faraway place to the target debris; the next is the measuring phase in which the rotation characteristics of the space debris are observed using the on-board measuring system; the third step is the capturing phase in which the target is captured by manipulating the robotic arm; the final step is the de-tumbling phase in which the relative rotation between the debris and the end effector is eliminated and then the whole system is de-tumbled or de-spun via thrust torque or other means.

An air-bearing testbed system is developed in this work to experimentally demonstrate the basic concept of debris capture, as shown in Fig. 2. The experimental system is mainly composed of a binocular camera, an image processing computer, a granite platform and two air-bearing simulators (ABS) floating on the granite platform via air-bearings. The chaser simulator (CS) is equipped with a single-degree-of-freedom robotic arm and the target simulator (TS) serves as a mock-up of the debris to be captured.

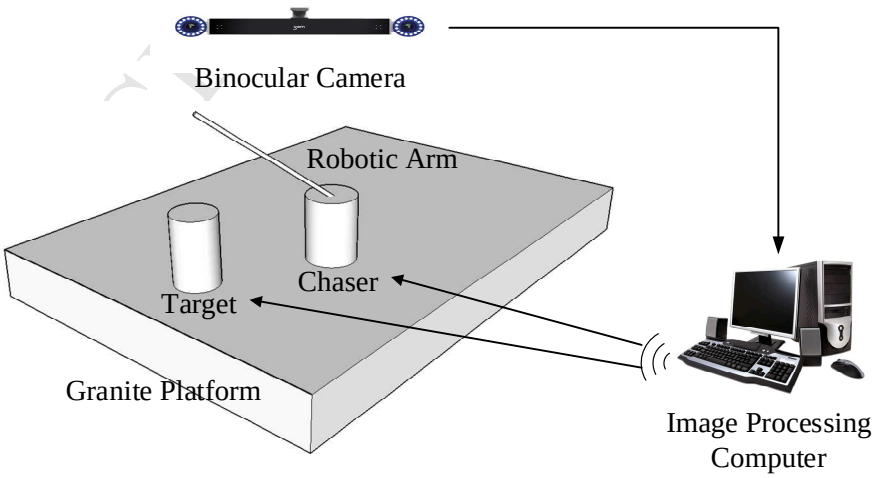

Fig. 2. The ground-based experiment system

As an initial proof of concept, the robotic arm in this work is simplified as a rod connected to CS through a single-degree-of-freedom revolute joint. The development of the adhesive end-effector is not considered in the represent work, and, for simplification, the free tip of the rod is equipped with a permanent magnet instead. A small piece of iron is fixed at the center of the top surface of TS, and the robotic arm of CS , as shown in Fig.3, is driven by a joint servo-motor and can be laid down to the horizontal plane for capturing TS at the position of the iron piece. With the consideration of the quite limited area of the granite table, TS is statically placed at a fixed position on the granite table and treated as a resident object to simplify the experimental implementation.

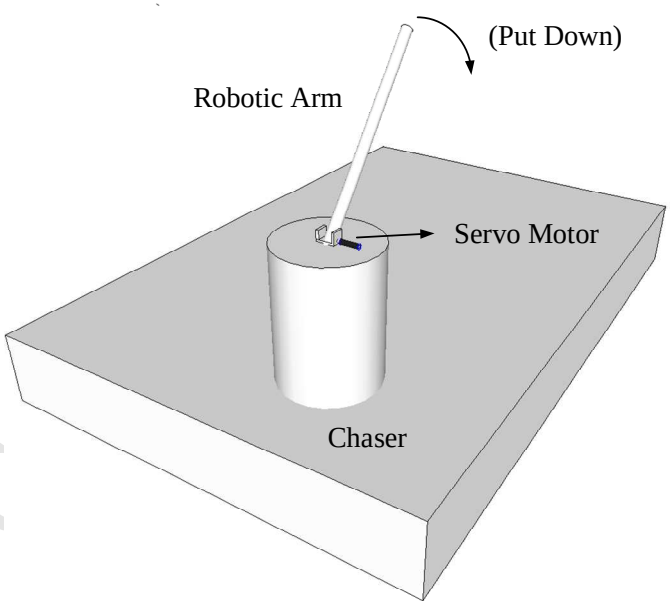

Fig. 3. The robotic arm driven by joint motor

As shown in Fig. 4, two coordinate systems are employed for the dynamic modeling of the ground-based experimental system: the inertial frame *OXY* and the body-fixed frame $o_1x_1y_1$ of CS. The attitude angle of CS with respect to the OX axis is denoted by θ_1. The radius of the ABSs is R and the length of the arm is

$L+2R$. The coordinate vector of point o_i is denoted by $\mathbf{r}_i = \left[X_i, Y_i\right]^{\mathrm{T}}$ for $i=1,2$, where X_i and Y_i represent the *X* and *Y*-coordinates of the center of the top surface of the two ABSs, respectively. The angle between the robotic arm and the o_1x_1-axis is $\alpha = 7\pi/6$, when the robotic arm is laid down to the horizontal plane. The solid line indicates the position vectors of the robotic arm when laid horizontally, and the black dots represent fluorescent markers for vision-based tracking. For the sake of clarity, introduce a virtual point C with the following absolute coordinates

$$\mathbf{r}_c = [X_1 + (L+2R)\cos(\theta_1+\alpha),\quad Y_1 + (L+2R)\sin(\theta_1+\alpha)]^{\mathrm{T}} \tag{1}$$

which coincides with the position of the free tip of the robotic arm when laid horizontally.

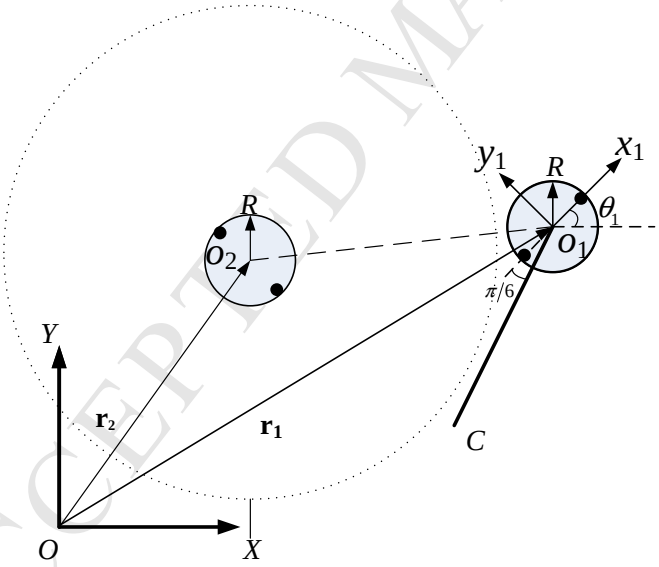

Fig. 4. Definitions of inertial and body-fixed reference frames

To achieve the capture of TS, the following maneuvering phases were implemented, as shown in Fig. 5. In phases a and b, CS approaches to TS from the edge of the granite platform by adjusting its attitude and location in real-time. In phase c, CS arrives at the pre-capture state such that the position of the virtual point C

coincides with that of the center of the top surface of TS. Finally, in phase d, the robotic arm is laid down to capture TS.

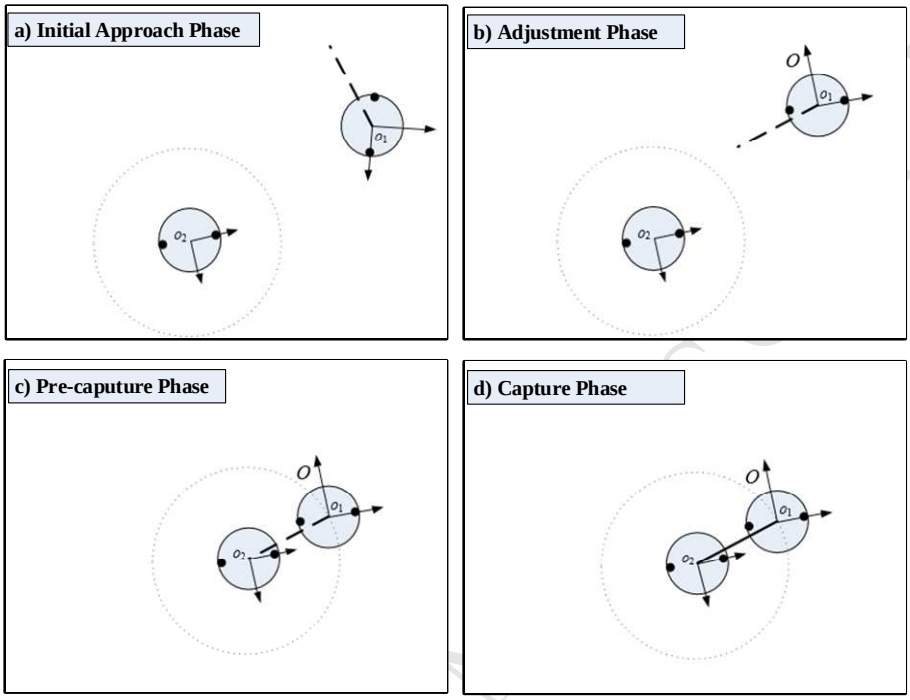

Fig. 5. The four phases of the capture mission on the air-bearing test bed

Orbital motions and perturbations are neglected in the following analysis because the capture is completed in a relatively short period of time. The kinetic energy of CS can be written as follows

$$T = \frac{1}{2}\dot{\mathbf{r}}_1^{\mathrm{T}} m_1 \dot{\mathbf{r}}_1 + \frac{1}{2} J_1 \dot{\theta}_1^2 \tag{2}$$

where m_1 and J_1 are the mass and the rotary inertia of CS, respectively. According to the Lagrange equation of the second kind, the dynamic equation of CS can be derived as

$$\mathbf{M}\ddot{\mathbf{q}} = \mathbf{u}_1 \tag{3}$$

where $\mathbf{M} = \mathrm{diag}\left[m_1 \quad m_1 \quad J_1\right]$ is the inertia matrix, $\mathbf{q} = \left[X_1 \; Y_1 \; \theta_1\right]^{\mathrm{T}}$ is the

generalized coordinate vector, and $\mathbf{u}_1 = \left[F_{1x}\ F_{1y}\ T_1 \right]^{\mathrm{T}}$ is the generalized external force vector which consists of the forces acting on CS's center in the X and Y direction and the moment acting on CS.

3. Controller Design and Stability Analysis

The control problem of current concern is to maneuver the chaser simulator such that the position of the virtual point C gets equal to that of the center of the top surface of TS. The pursued control objective is to guarantee, if the robotic arm is laid down to the horizontal plane, the free tip of the robotic arm can be exactly positioned at the center of the top surface of TS.

3.1 The design of the controllers

In the planar case, $\mathbf{x}=\left[X_1, Y_1, \theta_1, \dot{X}_1, \dot{Y}_1, \dot{\theta}_1 \right]^{\mathrm{T}}$ denotes the system state of CS at time t. The desired trajectory of the center of the top surface of CS is represented by the dotted line circle in Fig. 4, which ensures that the distance between the centers of the top surface of CS and TS is equal to $L+2R$, the length of the robotic arm. The attitude angle θ_1 of CS is given by

$$\theta_1 = 2\arctan\left[\delta y / \left(\delta x + \sqrt{\delta x^2 + \delta y^2} \right) \right] \tag{4}$$

where $\mathbf{d} = \left[\delta x, \delta y \right]^{\mathrm{T}}$ is the relative position of two fluorescent markers on CS in the inertial frame OXY. Hence, $\theta_1 \in \left(-\pi, \pi \right)$, i.e., there exists a singular point when $\theta_1 = -\pi$ or $\theta_1 = \pi$.

A potential-energy based control algorithm is devised based on the artificial potential field method to achieve the desired maneuvers of CS [26-28]. The artificial potential function, defined to adjust the position and attitude of CS, is defined as

follows

$$V^* = \beta[(X_1 - X_2)\sin(\theta_1 + \alpha) - (Y_1 - Y_2)\cos(\theta_1 + \alpha)]^2 + \left[r - \left(L + 2R\right)\right]^2 \tag{5}$$

where β is a positive coefficient and $r = \sqrt{\left(X_1 - X_2\right)^2 + \left(Y_1 - Y_2\right)^2}$. Accordingly, the potential-energy controllers based for position regulation can be formulated as

$$\begin{aligned} F_{1x} &= -K_1 \frac{\partial V^*}{\partial X_1} - K_2 \dot{X}_1 \\ F_{1y} &= -K_1 \frac{\partial V^*}{\partial Y_1} - K_2 \dot{Y}_1 \end{aligned} \tag{6}$$

where the coefficients K_1 and K_2 are positive coefficients. Besides, the potential-energy based controller for attitude regulation is designed as

$$T_1 = -K_1 \frac{\partial V^*}{\partial \theta_1} - K_3 \dot{\theta}_1 \tag{7}$$

where K_3 is also a positive coefficient. It is worth noting that the values of $\sin(\theta_1 + \alpha)$ and $\cos(\theta_1 + \alpha)$ can be directly determined by using δx and δy, thereby free of the singular problem of solving θ_1 using Eq. (4).

3.2 The stability analysis of the controllers

To facilitate the analysis, one defines

$$v_1 = (X_1 - X_2)\sin(\theta_1 + \alpha) - (Y_1 - Y_2)\cos(\theta_1 + \alpha) \tag{8}$$

$$v_2 = r - \left(L + 2R\right) \tag{9}$$

Theorem 1. All of the stable minima of the potential function defined in Eq. (5) correspond to the capturing condition that $v_1 = v_2 = 0$.

Proof: The first-order derivatives of the potential function with respect to the three coordinates are set as zero to obtain the extremum, namely

$$\frac{\partial V^*}{\partial X_1} = 2\beta v_1 \frac{\partial v_1}{\partial X_1} + 2v_2 \frac{\partial v_2}{\partial X_1} = 0 \tag{10}$$

$$\frac{\partial V^*}{\partial Y_1} = 2\beta v_1 \frac{\partial v_1}{\partial Y_1} + 2v_2 \frac{\partial v_2}{\partial Y_1} = 0 \tag{11}$$

$$\frac{\partial V^*}{\partial \theta_1} = 2\beta v_1 \frac{\partial v_1}{\partial \theta_1} = 0 \tag{12}$$

It is easy to verify that

$$\frac{\partial v_2}{\partial X_1}(Y_1 - Y_2) = \frac{\partial v_2}{\partial Y_1}(X_1 - X_2) \tag{13}$$

$$\frac{\partial v_1}{\partial \theta_1} = \frac{\partial v_1}{\partial X_1}(Y_1 - Y_2) - \frac{\partial v_1}{\partial Y_1}(X_1 - X_2) \tag{14}$$

Thus, it is obvious that the solution of Eqs. (10)-(12) should satisfy either of the following two conditions:

Condition A:

$$\begin{cases} v_1 = 0 \\ v_2 = 0 \end{cases} \tag{15}$$

Condition B:

$$\begin{cases} \dfrac{\partial v_1}{\partial X_1}(Y_1 - Y_2) - \dfrac{\partial v_1}{\partial Y_1}(X_1 - X_2) = 0 \\ X_1 - X_2 = \pm \dfrac{(L+2R)\sin(\theta_1 + \alpha)}{\beta + 1} \end{cases} \tag{16}$$

among which Condition B also implies $r = (L+2R)/(\beta+1)$. Note that $V^* \geq 0$ all the time, thus, it is easy to conclude that V^* arrives at its minimum if Eq. (15) is satisfied. It should be noted that Condition A defined in Eq. (15) implies that the position of the virtual point C coincides with that of the center of the top surface of TS. On the other hand, the Hessian matrix of V^* is examined to determine whether the solution of Eq. (16) is the stable minimum of V^*. The simplified Hessian matrix of V^* is

$$\boldsymbol{H}^* = 2\begin{pmatrix} (-2\beta-1)\cos\varphi^2+\beta+1 & (-2\beta-1)\sin\varphi\cos\varphi & -\dfrac{\beta\rho}{\beta+1}\cos\varphi \\ (-2\beta-1)\sin\varphi\cos\varphi & (2\beta+1)\cos\varphi^2-\beta & -\dfrac{\beta\rho}{\beta+1}\sin\varphi \\ -\dfrac{\beta\rho}{\beta+1}\cos\varphi & -\dfrac{\beta\rho}{\beta+1}\sin\varphi & -\dfrac{\beta\rho^2}{(\beta+1)^2} \end{pmatrix} \tag{17}$$

where $\varphi = \theta_1 + \pi/6$ and $\rho = L + 2R$. The eigenvalues of the Hessian matrix are $-2\beta\left(\rho^2+\beta^2+2\beta+1\right)/(\beta+1)^2$, 0 and $2\beta+2$, respectively. Consequently, under the Condition B defined in Eq. (16), the solution of Eq. (13) is the unstable saddle point of V^*. Thus, the stable minimum of V^* is uniquely defined by Eq. (15), thereby avoiding the possibility of trapping into any unwanted local minima.

Theorem 2. CS under the control laws (6) and (7) is asymptotically stable

Proof: Denote the solution of $\dfrac{\partial V^*}{\partial \mathbf{q}} = 0$ as $\mathbf{q}_s = \begin{bmatrix} X_{1s} & Y_{1s} & \theta_{1s} \end{bmatrix}^{\mathrm{T}}$, which satisfies the dynamic model. A candidate of the Lyapunov function is constructed as follows

$$L_v = \frac{1}{2}J_1\dot{\theta}_1^2 + \frac{1}{2}m_1\left(\dot{X}_1^2+\dot{Y}_1^2\right) + K_1V^* \tag{18}$$

Obviously, $L_v \geq 0$ always holds. $L_v = 0$ if and only if $V^* = 0$ and the generalized velocity vector of CS is equal to the zero vector. Consider the first derivative with respect to time of L_v

$$\dot{L}_v = J_1\dot{\theta}_1\ddot{\theta}_1 + m_1\dot{X}_1\ddot{X}_1 + m_1\dot{Y}_1\ddot{Y}_1 + K_1\dot{V}^* \tag{19}$$

Combining the control laws (6) and (7), Eq. (19) can be simplified as

$$\dot{L}_v = -K_2\dot{X}_1^2 - K_2\dot{Y}_1^2 - K_3\dot{\theta}_1^2 \tag{20}$$

which is always less than or equal to zero. Thus, the dynamics of CS is asymptotically stable under the control laws (6) and (7).

To evaluate the performance of the control scheme, numerical case studies are performed in MATLAB using the numerical integrator ode45. The length L was taken to be 0.3 m, and the mass, the rotational inertia and the radius of CS were set as 9 kg, 0.05 kgm^2 and 0.1 m, respectively. The control parameters β, K_1, K_2, and K_3 were set as 1, 4, 5, and 3, respectively.

Note that the stable minima defined in Eq. (15) are not unique but all correspond to the capture condition and, consequently, the final location of CS depends on its initial condition. Hence, two different initial states of CS are used in case studies for comparison. The two initial states of CS were taken to be $\left[X_1, Y_1, \theta_1, \dot{X}_1, \dot{Y}_1, \dot{\theta}_1\right] = [0.2, 0.3, 0, 0, 0, 0]$ and $[0.3, 0.3, 0, 0, 0, 0]$, respectively. TS statically resides at the position $[X_2, Y_2] = [0, 0]$. Figure 6 depicts the simulation results for a period of 50 seconds. Clearly, the position and attitude of CS achieve a stable state in approximately 15 and 10 seconds, respectively. By checking the value of X_1, Y_1 and θ_1, it is found that the artificial potential function is practically equal to zero and the capture condition is satisfied, which implies that the free tip of the robotic arm is at the center of the top surface of TS when the robotic arm is laid down to the horizontal plane.

ACCEPTED MANUSCRIPT

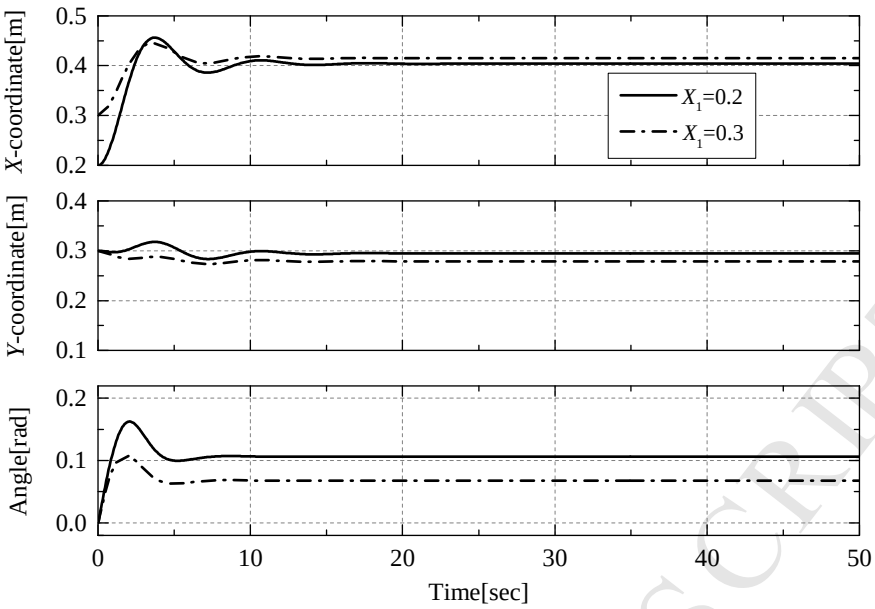

Fig. 6. Dynamic responses of CS subject to two different initial conditions

4. Ground-based Experiments

The proposed control algorithm is further validated experimentally based on the air-bearing testbed shown in Fig. 2. CS is equipped with a single-degree-of-freedom robotic arm and TS serves as a mock-up of the debris to be captured. Each satellite simulator is equipped with four normal and four tangential cold-gas thrusters to produce the normal forces and torque, respectively. Figure 7 shows the hardware layout of the ABSs.

ACCEPTED MANUSCRIPT

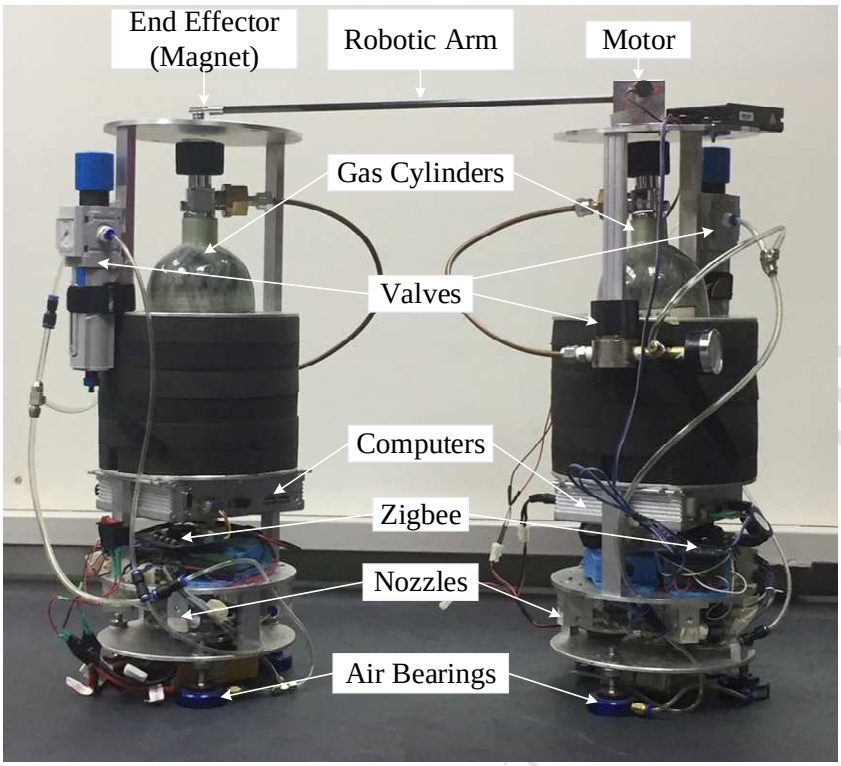

Fig. 7. The hardware layout of the two air-bearing simulators

The main part of the ABS weighs about 9 kg which includes about 1 kg of CO_2 in an on-board gas cylinder. The nominal pressure in the gas tank is about approximately 7 MPa. After flowing through the first stage decompression valve, CO_2 are divided into two-ways with the same pressure about 0.6 MPa. One pipe is directly connected to the three air bearings to allow the ABS to float above the granite platform, and the other pipe goes through the filter valve, which further reduces the pressure to about 0.2 MPa, to supply the eight nozzles, as shown in Fig. 8. Note that the electromagnetic valve used to control the nozzle switch is sensitive to the impurities in CO_2, therefore, the filter valve is necessary. In addition, the filter valve could ensure that the air supply pressures to the nozzles almost keep constant with different input pressures of the filter valve. For the given pressure 0.2 MPa, a normal

nozzle could provide a thruster force of about 0.05 N and a pair of tangential nozzles could generate the torque of about 0.008 Nm.

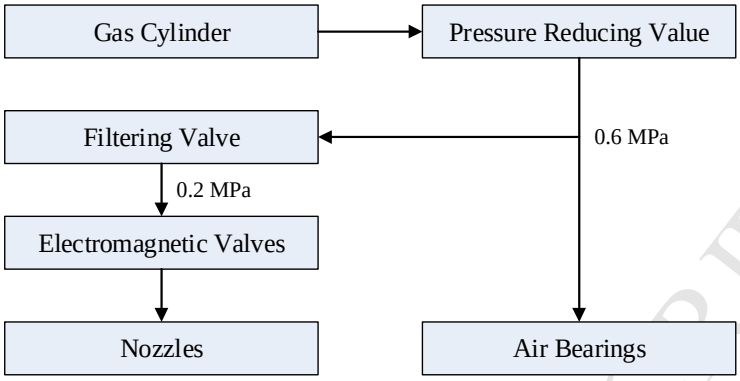

Fig. 8. Schematic view of the on-board cold gas system

As aforementioned, a single degree-of-freedom robotic arm is used in this paper. The robotic arm, which is driven by a servo motor, is a carbon fiber tube with a length of 50 cm, and its end effector is a permanent magnet. Because of the structural design, the robotic arm can only rotate in a fixed direction relative to CS. An on-board computer in the middle stage of the ABS and an on-board power system at the bottom of the ABS allow it to work without external dependencies. The ABS communicates with the image processing computer via a ZigBee module. Compared to the Wi-Fi module used by [29], the ZigBee module has lower power consumption and requires smaller battery capacity to achieve a longer usage time. As shown in Fig. 9, four fluorescent markers are placed on the top of the ABSs for the sake of optical measurement.

ACCEPTED MANUSCRIPT

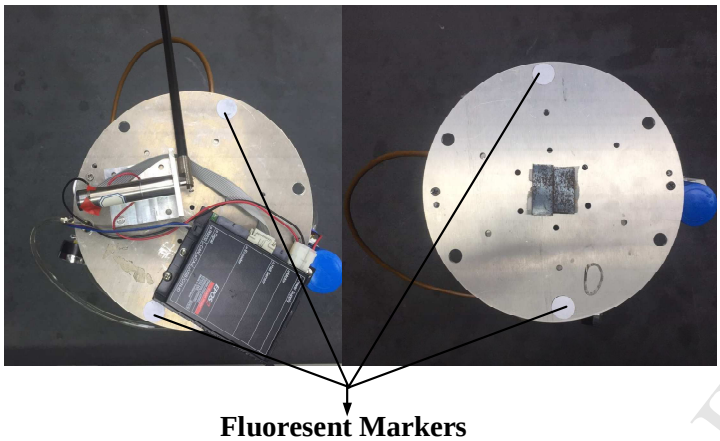

Fig. 9. Fluorescent markers at the top of ABSs

The positions of the fluorescent markers are captured in real-time by the binocular camera installed on the ceiling; subsequently, the acquired image data is further transmitted to the image processing computer. Whenever the computer obtains the three-dimensional coordinates by processing the digital image, it sends the information to the on-board computer mounted on the ABS via ZigBee wireless communication. According to the 3D coordinates of the markers, the feedback control law is solved by the on-board computer. By modulating the continuous control law by the Pulse Width/Pulse Frequency (PWPF) method [30], the switch command sequence for controlling the electromagnetic valves is obtained. Figure 10 shows the work flow chart of in the ground-based experimental system. It is worth noting that the single-degree-of-freedom robotic manipulator is also controlled by the on-board computer. Once the condition $\|\mathbf{r}_C - \mathbf{r}_2\| \le 0.02\,\mathrm{m}$ is satisfied for more than 10 s, the robotic arm is put down to capture TS.

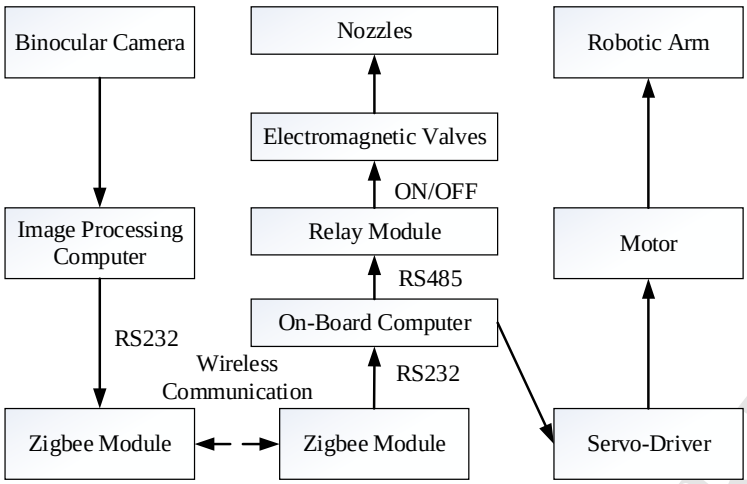

Fig. 10. The work flow chart of the experimental system

The experimental test is performed over a period of 60 seconds. The experimental results shown in Figs. 11-14 are obtained using the binocular camera and the image processing system. TS resides statistically at the positions (0.238, -0.090) m in the inertial frame used for optical measurement. The control parameters K_1, K_2, β and K_3 were set as 24, 50, 2 and 1, respectively.

Figures 11 and 12 depict the absolute coordinates of the virtual point C, where the dotted line represents the position of the center of TS. The coordinates of the virtual point C fluctuate slightly back and forth near the target value, due to the limited precision of the PWPF modulation of the thrust, as shown in the Figs. 11 and 12. However, the range of the coordinate fluctuation of the virtual point C is so small and does not affect the capture task. It can be found from Fig. 13 that the value of v_1 converges to zero with slight fluctuations. As shown in Fig. 14, the relative distance between the centers of the chaser and target is close to 0.8 m at the initial moment, and gradually converges to the target value. After $t = 40$ s, the relative distance remains at approximately 0.5 m and the capture condition $\|\mathbf{r}_C - \mathbf{r}_2\| \le 0.02$ m is met.

Finally, the capture task can be completed by laying down the robotic arm to place its free tip at the center of the top surface of TS.

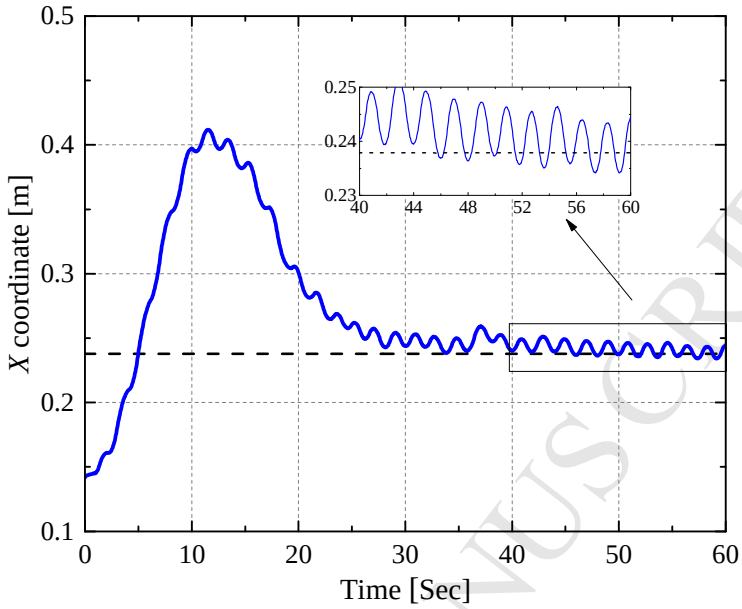

Fig. 11. The *X* coordinate of the virtual point C

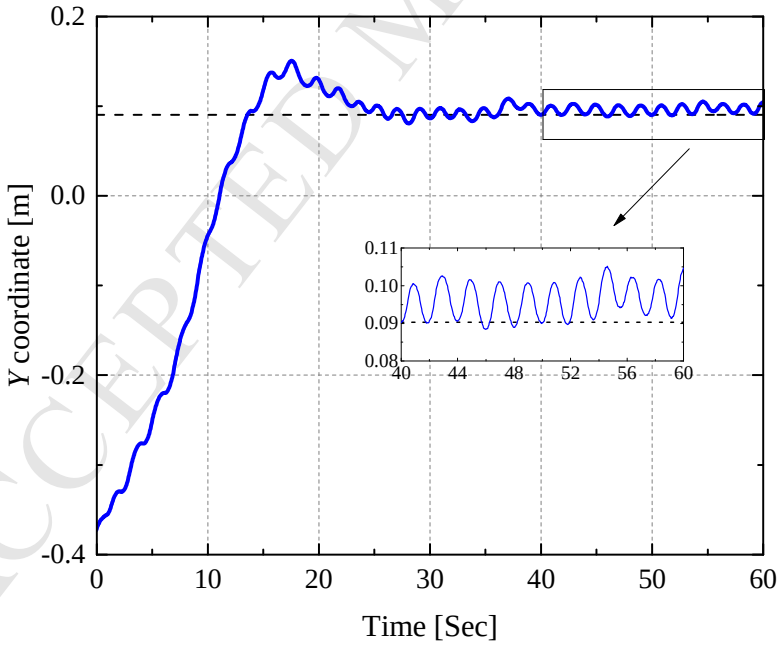

Fig. 12. The *Y* coordinate of the virtual point C

ACCEPTED MANUSCRIPT

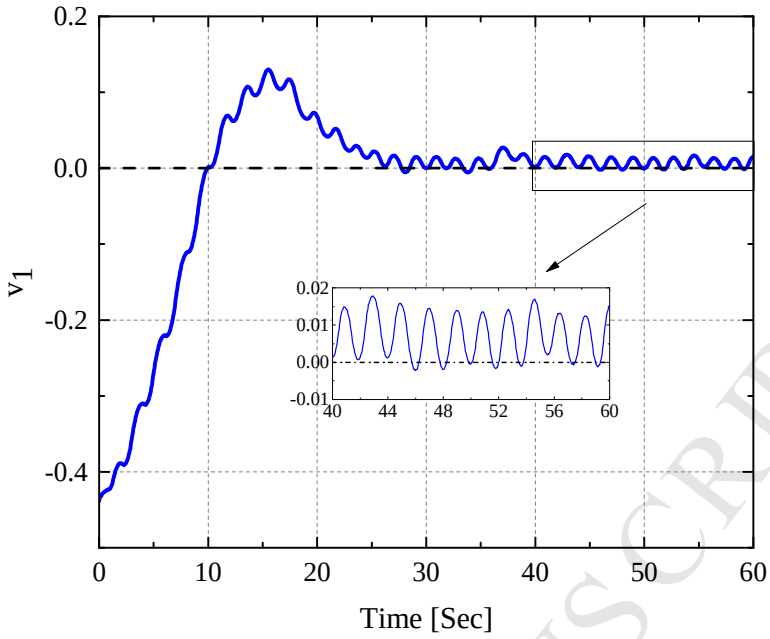

Fig. 13. The time history of v_1

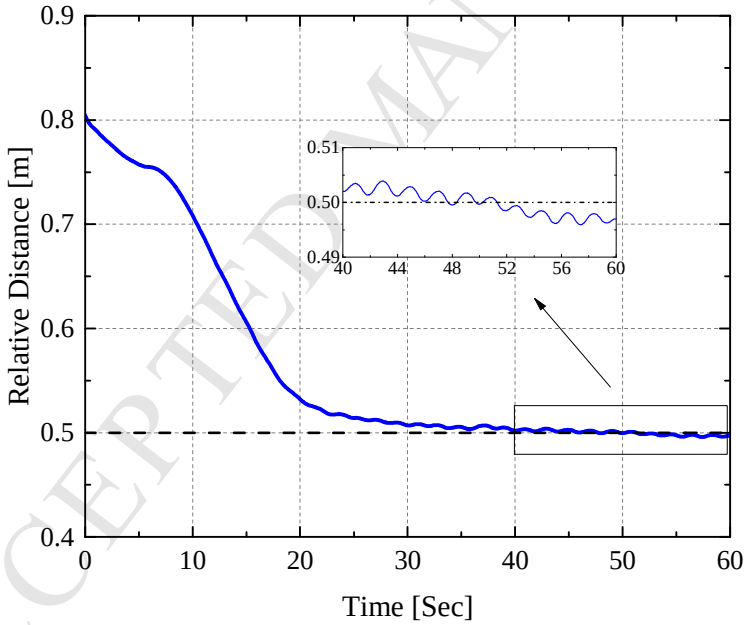

Fig. 14. The relative distance between the centers of the two ASs

5. Conclusions

Numerical and experimental studies are performed to demonstrate an enabling debris capturing concept based on the robotic arm on-board a chaser spacecraft. The experimental system has a chaser simulator equipped with a robotic arm and a target

simulator as a mock-up of the debris. The robotic arm is simplified in this work as a rod connected to the chaser simulator through a single-degree-of-freedom revolute joint. The position and attitude controller of the chaser simulator is synthesized using the method of artificial potential field such that the free tip of the robotic arm can be exactly positioned at the center of the top surface of the debris simulator to achieve a successful capture. The artificial potential function is constructed to avoid the possibility of trapping into any unwanted local minima, and the Lyapunov method is applied to demonstrate the asymptotically stability of the control scheme. The results of the numerical and experimental studies well demonstrate the efficiency and performance of the proposed control scheme. The proposed concept and scheme are currently verified using a simplified model which only accounts for the two-dimensional system motions and a single degree-of-freedom robotic arm. Significant extensions are required to handle the challenges of more realistic scenarios, such as the relative motions in the three-dimensional space, the complex dynamics of multiple degree-of-freedom robotic arm with adhesive effector and the pose estimation of non-cooperative targets.

Acknowledgments

This work was supported by the National Natural Science Foundation of China under Grant 11372130, and the Civil Aerospace Pre-research Project of China.

References:

[1] C. Bonnal, J. Ruault, M. Desjean, Active debris removal: Recent progress and current trends. Acta Astronautica, 2013, 85(4): 51-60.

[2] D.J. Kessler, B.G. Cour-Palais, Collision frequency of artificial satellites: the creation of a debris belt. Journal of Geophysical Research, 1978, 83(A6): 2637-2646.

[3] J.C. Liou, N.L. Johnson, Planetary science - Risks in space from orbiting debris. Science, 2006, 311(5759): 340-341.

[4] J.C. Liou, N.L. Johnson, N.M. Hill, Controlling the growth of future LEO debris populations with active debris removal. Acta Astronautica, 2010, 66(5): 648-653.

[5] Y. Lee, The problem of space debris and the environmental protection in outer space law. The Korean Journal of Air & Space Law and Policy, 2014, 29(2): 207-239.

[6] H. Wen., Z.H. Zhu, D.P. Jin, et al., Constrained tension control of a tethered space-tug system with only length measurement. Acta Astronautica, 2016, 119: 110-117.

[7] M. Jankovic, J. Paul, F. Kirchner, GNC architecture for autonomous robotic capture of a non-cooperative target: Preliminary concept design. Advances in Space Research, 2016, 57(8): 1715-1736.

[8] M. Shan, J. Guo and E. Gill, Review and comparison of active space debris capturing and removal methods. Progress in Aerospace Sciences, 2016, 80: 18-32.

[9] S. Ferraris, S. Perero, G. Gautier di Confiengo, et al., Friction, mechanical and ageing properties of surface modified materials for space debris capture. Advances in Space Research, 2016, 57(5): 1177-1188.

[10] F. Aghili, A prediction and motion-planning scheme for visually guided robotic capturing of free-floating tumbling objects with uncertain dynamics. IEEE Transactions on Robotics, 2012, 28(3): 634-649.

[11] W. Golebiowski, R. Michalczyk, M. Dyrek, et al., Validated simulator for space debris removal with nets and other flexible tethers applications. Acta Astronautica, 2016, 129: 229-240.

[12] M.K. Macauley, The economics of space debris: Estimating the costs and benefits of debris mitigation. Acta Astronautica, 2015, 115: 160-164.

[13] P.F. Huang, D. Wang, Z. Meng, et al., Impact dynamic modelling and adaptive target capturing control for tethered space robots with uncertainties, IEEE/ASME Transactions on Mechatronics, 2016, 21(5): 2260-2271.

[14] P.F. Huang, F. Zhang, Z. Meng, et al., Adaptive control for space debris removal with uncertain kinematics, dynamics and states. Acta Astronautica, 2016, 128: 416-430.

[15] W. Xu, B. Liang, C. Li, et al., A modelling and simulation system of space robot for capturing non-cooperative target. Mathematical and Computer Modelling of Dynamical Systems, 2009, 15(4): 371-393.

[16] H.Y. Lin, C.Y. Zhao, M.J. Zhang, Frequency analysis of the non-principal-axis rotation of uniaxial space debris in circular orbit subjected to gravity-gradient torque. Advances in Space Research, 2016, 57(5): 1189-1196.

[17] Q. Hu, J. Zhang, Dynamics and trajectory planning for reconfigurable space multibody robots. Journal of the Mechanical Design, 2015, 137.

[18] G. Dong, Z.H. Zhu, Autonomous robotic capture of non-cooperative target by adaptive extended Kalman filter based visual servo. Acta Astronautica, 2016, 122: 209-218.

[19] G. Dong, Z.H. Zhu, Incremental inverse kinematics based vision servo for autonomous robotic capture of non-cooperative space debris. Advances in Space Research, 2016, 57(7): 1508-1514.

[20] C. Toglia, F. Kennedy, S. Dubowsky, Cooperative control of modular space robots. Autonomous Robots, 2011, 31(2-3): 209-221.

[21] P. Boning, S. Dubowsky, Coordinated control of space robot teams for the on-orbit construction of large flexible space structures. Advanced robotics, 2010, 24(3): 303-323.

[22] J. Virgili-Llop, C. Zagaris, R. Zappulla, et al., Laboratory experiments on the capture of a tumbling object by a spacecraft-manipulator system using a convex-programming-based guidance. AAS/AIAA Astrodynamics Specialist Conference, Stevenson, WA, 2017.

[23] K. Zhang, X. Hou, P. Cao, et al., Research on the adhesion characteristic of climbing robot feet with bionic gecko microarray for spacecraft based on DEM. International Conference on Control, Nagoya, Japan, 2017: 206-211.

[24] K. Jin, J.C. Cremaldi, J.S. Erickson, et al., Biomimetic bidirectional switchable adhesive inspired by the gecko. Advanced Functional Materials, 2014, 24(5): 574-579.

[25] H. Jiang, E.W. Hawkes, C. Fuller, et al., A robotic device using gecko-inspired adhesives can grasp and manipulate large objects in microgravity. Science Robotics, 2017, 2(7): eaan4545.

[26] T. Chen, H. Wen, H.Y. Hu, et al., On-orbit assembly of a team of flexible spacecraft using potential field based method. Acta Astronautica, 2017, 133: 221-232.

[27] H. Wen, T. Chen, D.P. Jin and H.Y. Hu, Passivity-based control with collision avoidance for a hub-beam spacecraft. Advances in Space Research, 2017, 59(1): 425-433.

[28] T. Chen, H. Wen, Autonomous assembly with collision avoidance of a fleet of flexible spacecraft based on disturbance observer. Acta Astronautica, 2018, 147: 86-96.

[29] R. Bevilacqua, J.S. Hall, J. Horning, et al., Ad hoc wireless networking and shared computation for autonomous multirobot systems. Journal of Aerospace Computing Information and Communication, 2009, 6(5): 328-353.

[30] G. Guglieri, F. Maroglio, P. Pellegrino, et al., Design and development of guidance navigation and control algorithms for spacecraft rendezvous and docking experimentation. Acta Astronautica, 2014, 94(1): 395-408.

ACCEPTED MANUSCRIPT

ACCEPTED MANUSCRIPT

Highlights:

1) The control scheme is synthesized using artificial potential field.
2) The constructed artificial potential function is free of unwanted local minima.
3) The proposed scheme is experimentally demonstrated using an air-bearing testbed.

ACCEPTED MANUSCRIPT